Effect of interfacial interdiffusion on magnetism in epitaxial Fe$_4$N films on LaAlO$_3$ substrates

Nidhi Pandey,[1] S. Pütter,[2] S. M. Amir,[2] V. R. Reddy,[1] D. M. Phase,[1] J. Stahn,[3] Ajay Gupta,[4] and Mukul Gupta ⊙[1,*]

[1]*UGC-DAE Consortium for Scientific Research, University Campus, Khandwa Road, Indore 452 001, India*

[2]*Jülich Centre for Neutron Science (JCNS) at Heinz Mair-Leibnitz Zentrum (MLZ), Forschungszentrum Jülich GmbH, Lichtenbergstr. 1, 85748 Garching, Germany*

[3]*Laboratory for Neutron Scattering and Imaging, Paul Scherrer Institut, CH-5232 Villigen PSI, Switzerland*

[4]*Amity Center for Spintronic Materials, Amity University, Sector 125, Noida 201 303, India*

Epitaxial Fe$_4$N thin films grown on LaAlO$_3$ (LAO) substrate using sputtering and molecular beam epitaxy techniques have been studied in this work. Within the sputtering process, films were grown with conventional direct current magnetron sputtering (dcMS) and using a high power impulse magnetron sputtering (HiPIMS) process. Surface morphology and depth profile studies on these samples reveal that HiPIMS deposited film has the lowest roughness, the highest packing density, and the sharpest interface. We found that the substrate-film interface and the microstructure play a vital role in affecting the electronic hybridization and magnetic properties of Fe$_4$N films. La from the LAO substrate and Fe from the film interdiffuse and form an undesired interface. The magnetic moment (M_s) was compared using bulk, element-specific and magnetic depth profiling techniques. We found that M_s was the highest when the thickness of the interdiffused layer was lowest and such conditions can only be achieved in the HiPIMS grown samples. The presence of a small moment at the N site was also evidenced by element-specific x-ray circular dichroism measurement in the HiPIMS grown sample. A large variation in the M_s values of Fe$_4$N films found in the experimental works carried out so far could be due to such an interdiffused layer which is generally not expected to form in otherwise stable oxide substrate at a low substrate temperature ≈675 K. In addition, a consequence of substrate-film interdiffusion and microstructure resulted in the different kinds of magnetic anisotropies in Fe$_4$N films grown using different techniques. A detailed investigation of the substrate-film interface and microstructure on the magnetization of Fe$_4$N film is presented and discussed in this work.

I. INTRODUCTION

Thin films of ferromagnetic materials hold considerable potential in spintronic devices due to their several enticing properties [1–4]. The appropriate selection of film layer thickness, film structure, interfacial bonding, interface roughness, interdiffusion, and so forth, exquisitely governs the magnetic properties of thin films [5,6]. Among them, the interface formed with the substrate or a seed/buffer layer also plays a delicate role in optimizing the magnetic properties through break-in local symmetry, strain induced by substrate, or by interfacial morphology (interdiffusion, surface reconstruction, roughness) [2,4–6].

Nevertheless, the commonly encountered issues such as interdiffusion, interfacial roughness, or compound formation at the interface severely alter the magnetic properties of thin films. Therefore, understanding the correlation between interfacial interdiffusion and magnetic properties is not only of fundamental interest but is also necessary for the development of application devices.

Recently Fe$_4$N has also been recognized as a spin electronic material due to its excellent properties, such as high magnetic moment ($M_s \approx 2.4 \mu_B$/Fe atom [7]), high chemical stability, low coercivity, a high Curie temperature (≈761 K [8]), and a high spin polarization (spin polarization ratio; SPR ≈ 100% [9]). Meanwhile, this substance is also predicted to exhibit a giant value of TMR (≈24000%) due to the resonance tunneling and transmission of the spin band at the interface with MgO based heterostructure [10]. In addition, perpendicular magnetic anisotropy has also been found in the Fe$_4$N films [11–13]. Such demanding properties of Fe$_4$N enable it to serve as a switching electrode in the new generation of spintronics technologies.

However, the key to these eminent multifunctionalities relies crucially on the structure of the interfaces that seem to be obscured in Fe$_4$N films which can be seen in its associated magnetic phenomena and properties. For example, a large variation can be seen in the experimental M_s values of Fe$_4$N thin films studied so far (from the theoretical value of $2.35 \pm 0.1 \mu_B$/Fe atom; see Table I). In some studies, M_s as high as 2.9 μ_B [14] and as low as 1.3 μ_B/Fe atom [15] has been reported. In most other works, the M_s of Fe$_4$N was found between these two extremes as shown in Table I. Such a large scattering in the M_s values can emphatically arise due to the interfacial effects which can be related to the breaking of the symmetry or diffusion at the interfaces. Therefore, probing the detailed depth profile can be useful to understand the involved mechanism at the interface. Moreover, other factors such as (i) measurement accuracy, (ii) phase purity and/or

*Corresponding author: mgupta@csr.res.in

TABLE I. A comparison of Fe_4N films deposited using different methods: direct current/radio frequency (dc/rf) magnetron sputtering (MS), molecular beam epitaxy (MBE), electron-beam evaporation (e-beam) for their measured magnetic moment (M_s) obtained using corresponding magnetization measurements method such as bulk magnetization (bulk) and x-ray circular magnetic dichroism (XMCD) in different experimental works. For reference, theoretically calculated M_s of Fe_4N compound is also included.

M_s μ_B/Fe	Depsoition Method	Magnetization measurement	Reference
2.9	dcMS	bulk	[14]
2.6	dcMS	bulk	[14]
2.7	dcMS	bulk	[14]
1.3	dcMS	bulk	[15]
2.3	rfMS	bulk	[16]
2.64	MBE	bulk	[19]
2.47	MBE	XMCD	[19]
2.04	sputtering	bulk	[20]
2.1	e-beam	XMCD	[21]
2.12	MBE	bulk	[22]
1.65	sputtering	bulk	[23]
1.82	dcMS	bulk	[24]
1.48	dcMS	bulk	[24]
1.68	dcMS	bulk	[25]
2.35 ± 0.1		Theoretical	[7,8,26,27]

compositional variations across the depth of the film, and (iii) the deposition methodology affecting the microstructure may also be responsible for such deviation in the M_s values of Fe_4N thin films. These factors need to be sought which can open a new dimension to understand the magnetic behavior of Fe_4N.

It may be noted here that in most of the works reported so far, mainly the bulk magnetization measurements, have been performed on Fe_4N thin films (see Table I), which inherently includes the large foreseen errors while estimating the film volume.

Structural and magnetic depth profiling in Fe_4N films is also completely lacking. Moreover, different deposition methodology may also lead to different microstructure and hence different M_s values in Fe_4N thin film. Mostly, direct current magnetron sputtering (dcMS) [14–18] and molecular beam epitaxy (MBE) [19,28–31] methods have been extensively used to prepare the Fe_4N films, whereas a relatively new but very promising technique—high power impulse magnetron sputtering (HiPIMS)—has not yet been employed. There are several advantages inherent to the HiPIMS process over the conventional dcMS process such as improvement of the film quality by denser microstructure and enhanced adhesion etc. [32,33]. As compared to dcMS, in HiPIMS high-power pulses are employed at low duty cycle (<10%) [34] leading to enhanced ionization of process gas and sputtered species. Therefore, the fraction of ionized species exceeds neutrals. These unusual properties of HiPIMS led to additional improvement in the film quality [32,33].

In view of this, we scrutinize factors affecting the variation in M_s in a systematic way in this work. We deposited single-phase and epitaxial Fe_4N film on a $LaAlO_3$ substrate (lattice parameter; LP = 3.79 Å) as it is almost 100% lattice matched with Fe_4N ($LP = 3.79$ Å) [7]. They were deposited using three different techniques namely dcMS, N-plasma assisted MBE and HiPIMS. We performed detailed depth profiling measurements on these samples and found an interesting result that La from the LAO and Fe from Fe_4N interdiffuse at the film-substrate interface. The extent of this interface gets affected due to differences in the microstructure of samples grown using different methods. By further performing magnetic depth profiling and element-specific magnetization measurements, we attempt to understand the role of interface and microstructure in affecting the magnetization of Fe_4N thin films.

II. EXPERIMENTAL PROCEDURE

Fe_4N films were grown on $LaAlO_3$ (100) substrate using N-assisted MBE (DCA, M600 system at JCNS, Garching), direct current magnetron (dcMS), and high power impulse magnetron sputtering (HiPIMS) (ATC Orion 8, AJA Int. Inc. at UGC-DAE CSR, Indore) techniques. For MBE growth, N was provided by an rf plasma source at 0.07 standard cubic centimeter per minute (sccm) gas flow while Fe (99.95%) was evaporated from an effusion cell. The base pressure of the MBE system was about 2×10^{-10} Torr and during growth was about 1.3×10^{-7} Torr. In dcMS and HiPIMS processes, Fe targets (99.95% pure) $\phi 1$ inch and $\phi 3$ inch were used as a source, respectively. In the HiPIMS process, the peak power was maintained at 26 kW by keeping the average power fixed at 300 W, peak voltage 700 V, pulse frequency 75 Hz, and pulse duration 150 μs. In dcMS process, the sputtering power was fixed at 5 W. The partial gas flow of nitrogen ($R_{N_2} = p_{N_2}/(p_{Ar} + p_{N_2})$, where p_{Ar} and p_{N_2} are the gas flows of Ar and N_2 gases, respectively) was kept at 10 and 23% for dcMS and HiPIMS processes, respectively. A base pressure of 1×10^{-7} Torr was achieved before deposition and the working pressure was maintained at 4 mTorr during the deposition in both dcMS and HiPIMS processes. The thicknesses of Fe_4N samples were about 50 nm. An Au layer of thickness around 2 nm was used as a capping layer in MBE grown Fe_4N film.

The crystal structure and the phase formation of the films were characterized by x-ray diffraction (XRD) using a standard x-ray diffractometer (Bruker D8 Advance) using CuK-α x-ray source. Compositional depth profiling was performed using secondary ion mass spectroscopy (SIMS) in a Hiden Analytical SIMS workstation. A primary O_2^+ ions source was used for sputtering with an energy of 3 keV and beam current of 150 nA. The sputtered secondary ions were detected using a quadrupole mass analyzer. X-ray reflectivity measurements were carried out using a Cu K-α x-ray source. Bulk magnetization measurements were done using a Quantum Design SQUID-VSM magnetometer. Polarized neutron reflectivity (PNR) measurements were performed at AMOR, SINQ, PSI Switzerland in time of flight mode using Selene optics on samples deposited using dcMS and HiPIMS [35,36]. PNR measurements on MBE deposited samples were carried out using the magnetic reflectometer with high incident angle (MARIA) of the JCNS, Garching, Germany [37]. During PNR measurements, to saturate the sample magnetically, a
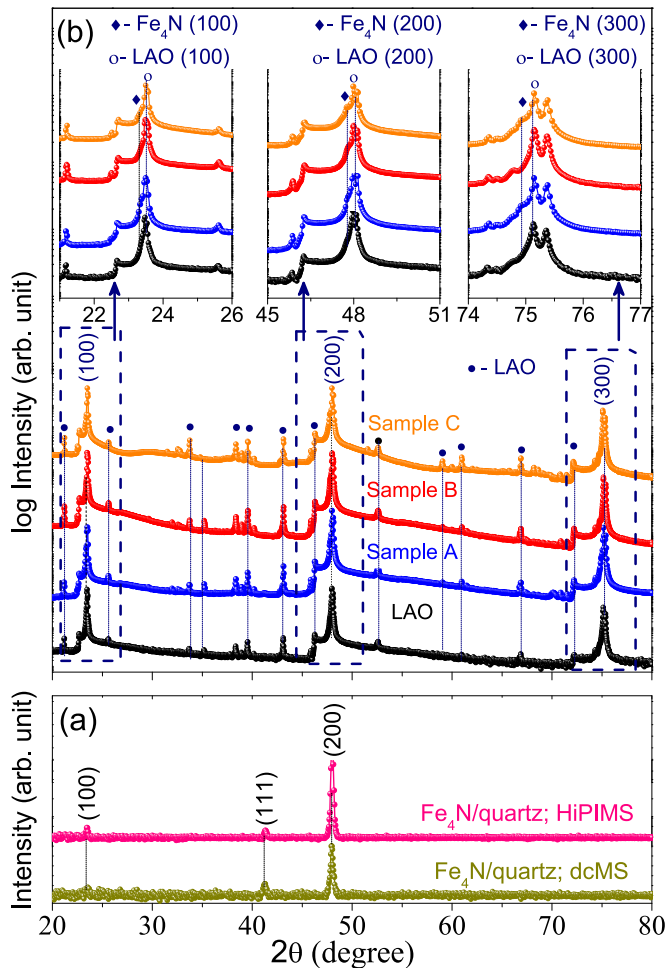
FIG. 1. XRD patterns of polycrystalline Fe_4N film deposited on quartz substrate using dcMS and HiPIMS (a). The y scale used in (a) is linear. XRD patterns of Fe_4N samples grown on LAO subtracts using dcMS (sample A), HiPIMS (sample B), and MBE (sample C) (b). For comparison the XRD pattern of a bare LAO substrate in also included in (b). The y scale used in (b) is logarithmic. In (b) along with reflections corresponding to (100), (200), and (300) planes of LAO, some faint reflections (also from LAO and marked by ●) can also be seen. The inset of (b) compares a magnified view in the vicinity of (100), (200), and (300) reflections.

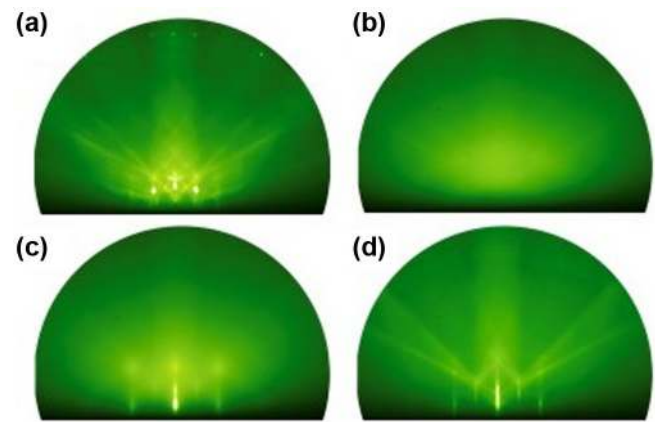FIG. 2. Evolution of the RHEED pattern during growth of Fe_4N on LAO (001) substrate (sample C). (a) LAO substrate before deposition and at different stages of Fe_4N growth, namely at thickness of about (b) 1.9 nm, (c) 2.6 nm, (d) 40 nm. The 15 keV electron beam was along the [110] direction.

magnetic field of 0.5 T was applied parallel to the sample surface. X-ray magnetic circular dichroism (XMCD) measurements were carried out at BL-01, Indus 2, RRCAT, India [38]. The x-ray incidence angle was fixed at 90° with respect to the sample surface. Magnetic anisotropy was studied using magneto-optical-Kerr effect (MOKE) and Kerr microscopy (Evico Magnetics) equipment.

III. RESULTS AND DISCUSSION

A. Structure and bulk magnetization

Fe_4N thin film samples grown on LAO(001) substrate are labeled as: dcMS (sample A), HiPIMS (sample B), and MBE (sample C) and their XRD patterns are shown in Fig. 1. For reference, XRD patterns of two polycrystalline Fe_4N films deposited along with the above-mentioned samples (grown on amorphous quartz substrate using dcMS and HiPIMS) and a bare LAO substrate are also included in Fig. 1(a). Polycrystalline samples demonstrate solely three peaks associated to (100), (111), and (200) planes of the Fe_4N. This implies the formation of a single Fe_4N phase. Furthermore, the XRD patterns of samples grown on the LAO substrate show no distinct reflections other than that the LAO substrate, shown in Fig. 1(b), confirms the formation of a single phased Fe_4N thin film. This could be understood from the fact that LAO and Fe_4N exhibit 0% lattice mismatching and therefore, discrimination between the peak positions of LAO and Fe_4N is not possible. In order to distinguish the reflection of Fe_4N phase, an enlarged view corresponding to (100), (200), and (300) peaks have been plotted as shown in the inset of Fig. 1(b). A shoulder appeared towards lower 2θ can be seen in each case confirming the presence of the Fe_4N phase. As expected, for a higher angled (300) plane, it is considerably noticeable rather than the lower angle planes. Consequently, our XRD results confirm the formation of a single phased Fe_4N film well oriented along the c axis (normal) of the substrate.

To examine the nature of growth, RHEED images were taken *in situ* (for MBE grown sample C) and are shown in Fig. 2, before (on bare LAO substrate) and after several deposition sequences. The RHEED image of the LAO (001) substrate matches well with those observed in the literature [39–41]. Features present here can be described as (i) splitting of diffraction spots due to the presence of twin structures and (ii) presence of Kikuchi lines and a Laue ring with sharp spots indicating high surface quality and crystallinity. As the Fe_4N film starts to grow, the RHEED pattern changes significantly and is shown for film thicknesses of about 1.9, 2.6, and 40 nm in Fig. 2. In the initial stage Fe_4N exhibits amorphous growth, Fig. 2(b). During growth of another nm of Fe_4N a RHEED pattern evolves with faint Kikuchi lines as shown in Fig. 2(c). The 2D streaky pattern indicates epitaxial growth. As the film thickness increases, the Kikuchi lines become more pronounced which signifies increasing crystallinity and homogenous film layer formation, Fig. 2(d). It can also be
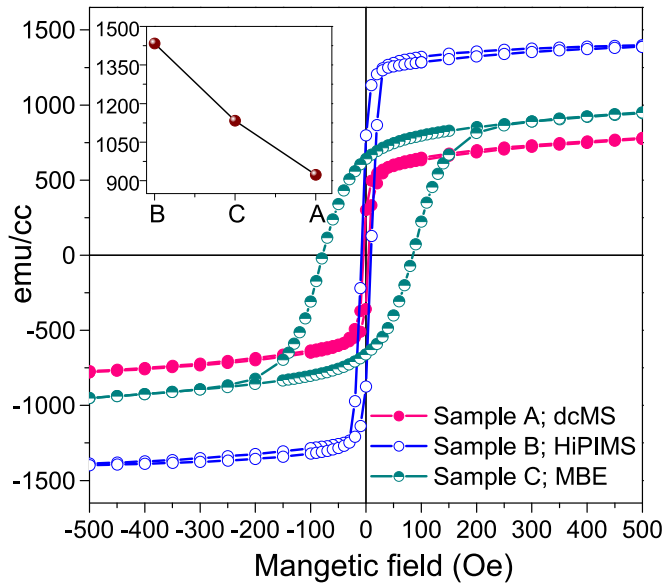
FIG. 3. In-plane MH hysteresis curves of samples A, B, and C. Inset showing the respective M_s values.

FIG. 4. SIMS depth profiles of Fe$_4$N thin films deposited on LAO substrate using dcMS (sample A), HiPIMS (sample B), and MBE (sample C) techniques. ^{57}Fe, ^{14}N, and ^{81}Al profiles (a), respective La profiles (b), and ^{57}Fe profiles (c) of samples A, B, and C are shown. The insets of (b) show the ln(^{138}La)-versus-$Z^{6/5}$.

seen that with successive increasing thickness, the RHEED 2D streaky pattern becomes sharper and more intense, indicating the enhancing crystallinity of the growing film. The RHEED pattern maintains an almost similar aspect until the end of the deposition of Fe$_4$N film. In addition, there is an indication for intensity modulation in the 2D streaks during growth, related to layer-by-layer growth [42]. It should also be noted here that the RHEED diffraction spots retain the same spatial distance during the film growth as the LAO substrate, which indicates the in-plane lattice is almost unchanged. This is expected because the lattice parameter of LAO and Fe$_4$N matches well at about 3.79 Å. Hereby, the RHEED images confirm the epitaxial growth of Fe$_4$N films. After completion of the Fe$_4$N deposition, the RHEED pattern of the Au capped sample exhibits polycrystallinity (not shown). Microstructure and surface morphology of these samples were obtained using atomic force microscopy (AFM) measurements shown in the Supplemental Material [43]. From here, it can be seen that HiPIMS grown samples exhibit a denser microstructure and lower roughness.

Bulk magnetization measurements were performed on all samples A, B, and C, and corresponding in-plane MH hysteresis loops are shown in Fig. 3. The coercivity (H_c) of samples A and B is comparable to the values previously obtained for Fe$_4$N films and corroborates its soft ferromagnetic nature. On the other hand, for sample C, it is much higher at about 100 Oe. The angle-dependent MOKE measurements (in-plane/out-of-plane; not shown here) negate the possible contribution from the anisotropic differences in the larger H_c of sample C. It may also be noted here that the MH hysteresis loop of sample C exhibits a clear remanence as well as readily gets saturation at a field of about 2400 Oe, demonstrating that magnetic domains are well aligned along the in-plane direction. Thus, the large H_c of sample C indicates the involvement of different types of interfaces. Film-substrate and film-capping interfaces present in sample C that may have
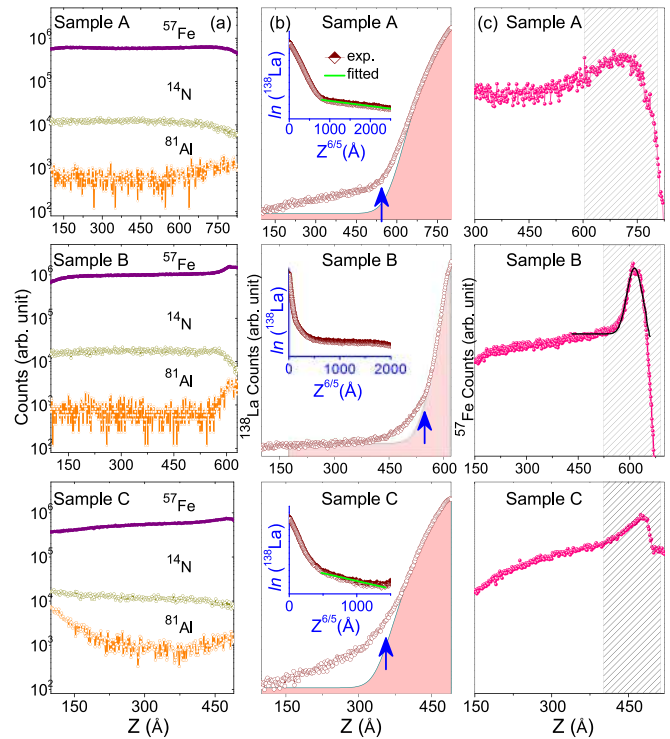
attributed to higher pinning domain resulted in larger H_c. Moreover, an even larger difference can be seen in the values of saturation magnetization (M_s) for samples A, B, and C shown in the inset of Fig. 3. M_s is the highest for sample B (HiPIMS) while the lowest for sample A (dcMS). However, even the highest obtained value of $M_s \approx 1425$ emu/cc for HiPIMS grown sample is still lower than its theoretical value ≈ 1690 emu/cc [7].

B. Structural and magnetic depth profiles of Fe$_4$N films

From our XRD measurements, it can be seen that the structure of samples grown using dcMS, HiPIMS, and MBE is similar and confirms the epitaxial growth of Fe$_4$N on LAO substrate. But from our bulk magnetization measurements and CEMS measurements [43], the overall values of M_s are smaller than the theoretically predicted values [7]. Differences in M_s values can also be seen in samples prepared using different techniques (see Table I). In order to understand such variances in M_s, we did elemental and magnetic depth profiling using SIMS and PNR, respectively.

SIMS depth profiles are shown in Fig. 4(a) for samples A, B, and C. Here, we can see that the Fe and N profiles demonstrate nearly uniform behavior and an analogous distribution with respect to each other along the depth (Z) of the films in samples A (dcMS) and B (HiPIMS), whereas, they seem to be skewed in sample C (MBE) near to the surface and interface regions. This reflects that the distribution of Fe and N is more uniform in samples A and B while there is the presence of

some concentration gradient in sample C. On the other hand, La depth profiles, shown in Fig. 4(b), reveal the mystery. We can see that at the film substrate boundary, the La counts do not rise abruptly but rather show a linear tail on the rising part of the inflection point [shown by arrow in Fig. 4(b)] accompanied by a Gaussian distribution in all three samples. This linear tail indicates La diffusion through grain boundaries [44–46] beyond the interface into the Fe_4N films. It is known that the slope of the linear relation between ln(SIMS counts) and $Z^{6/5}$ yields the grain boundary diffusion (D_g), if volume diffusion (D_v) is known [44–46].

$$\delta D_b = 1.322 \sqrt{\frac{D_v}{t}} \left(-\frac{\partial \ln c}{\partial Z^{6/5}} \right)^{-5/3} \quad (1)$$

where δ is the grain boundary width, c is SIMS concentration, and t is the annealing time.

Since the D_v cannot be calculated in the present case (as it requires detailed isothermal annealing at different temperatures) therefore, we can only qualitatively estimate the D_b in our case. In order to fit ln(^{138}La)-versus-$Z^{6/5}$, first, we need to make the peak of La profile at zero (nm) by subtracting the corresponding depth value in the rest of the depth. The ln(^{138}La)-versus-$Z^{6/5}$ curve for each La profile is linearly fitted [shown in the insets of Fig. 4(b)]. Here we can clearly see that the slope is higher in sample C (MBE grown Fe_4N) than in sample A. Hereby, our SIMS results reveal the dominant La diffusion into the Fe_4N film through larger grain boundaries present due to smaller grains (shown in AFM image Fig. 1; given in Supplemental Material [43]) in MBE grown sample C. Such La diffusion may also cause the gradient in concentration of Fe and N as found for sample C and discussed above.

Moreover, the film-substrate interdiffusion region is fitted with a Gaussian function and FWHM comes out to be about 20, 7, and 14 nm, for sample A, B, and C, respectively, and reflects the thinnest film-substrate interface in sample B (HiPIMS) while highest in sample A. In these results it is evident that La diffuses more into films through grain boundaries to a larger length scale quite substantially in dcMS and MBE grown samples (sample A and C) but not so much in sample B and also play a major role in forming a broad interface.

The diffusion of La into Fe_4N films can also be understood in terms of the interfacial excess. Interfacial excess ($Z^\star$) of a species is defined as the excess number density of atom caused by the interface. $Z^\star$ of reactive species at the interface has been proficiently quantified in the polymer glasses using SIMS measurements. The change in the $Z^\star$ reflects as an increase of concentration around the interface realm in the concentration depth profiles and has been fitted using Gaussian function, expressed as [47,48]:

$$Z^\star = 1.064 \times h \times \Delta \quad (2)$$

where h and Δ is the height and FWHM of the Gaussian peak.

In the present study also, we can see that the SIMS depth profile of ^{57}Fe shows a cusp/plateau near the film-substrate interface in all samples as shown by the shaded region in Fig. 4(c). This clearly reflects that the matrix effect for Fe sputtering is significantly modified here and results in variation in Fe sputtering yield. It is apparent from Fig. 4(c) that
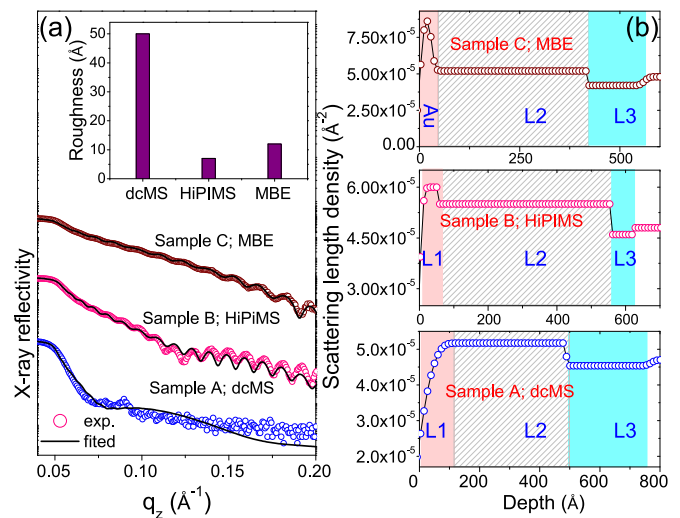

FIG. 5. XRR patterns (a) and SLD depth profiles (b) of samples A, B, and C. Inset of (a) showing the roughness of samples A, B, and C. Here, L1, L2, and L3 denoted the surface region, the bulk of the Fe_4N film and the film-substrate interface, respectively.

$Z^\star$ is highest in sample B while lowest in sample A. Using the height and FWHM obtained from the Gaussian fit of the shaded ^{57}Fe profile region [shown for sample B in Fig. 4(c)], it was found that $Z^\star$ is decreased by about 60 and 50%, respectively, for samples A and C, compared to sample B. It is also interesting to note here that the FWHM of the Gaussian peak correspond to the film-substrate interface region of La depth profile is the highest in sample A and the smallest in sample B, indicating that the higher the interfacial excess, the lower La diffusion. This clearly indicates that a densely packed region forms near the film-substrate interface in case of sample B which will act as a barrier to interrupt diffusion of La into the film. Thus, a relatively narrower film-substrate interface and inferior diffusion of La are observable for the HiPIMS grown sample.

Such interdiffusion of La has been previously probed in $SrTiO_3$/LAO heterostructures and it was found that La forms a broader interface (compared to Al in LAO) and has been described in terms of the stability of LAO compound with oxygen vacancies [49,50]. Oxygen depletion from LAO induces the Al diffusion into subsurface regions but a change of valency of La from 3^+ to 2^+ acts as a driving force leading to segregation of La to much larger length scales [50].

To further confirm SIMS results, depth profiles were also obtained from XRR measurements as shown in Fig. 5(a). Fitting of XRR data were performed (using Parraatt32 [51]) considering a three-layer model: (i) L1—surface region, (ii) L2—the bulk of Fe_4N film, and (iii) L3—film-substrate interface. As shown in Fig. 5(b), the width of L3 is substantially small in HiPIMS grown sample B as compared to samples A and C. This behavior is in agreement with SIMS depth profiling results and the width of the interface is also similar. As discussed before, such variations can be understood due to larger La interdiffusion when the microstructure is porous in dcMS and MBE grown samples but due to denser microstructure, La diffusion gets suppressed leading to sharper interface in the HiPIMS grown sample. In addition, it can be seen that surface
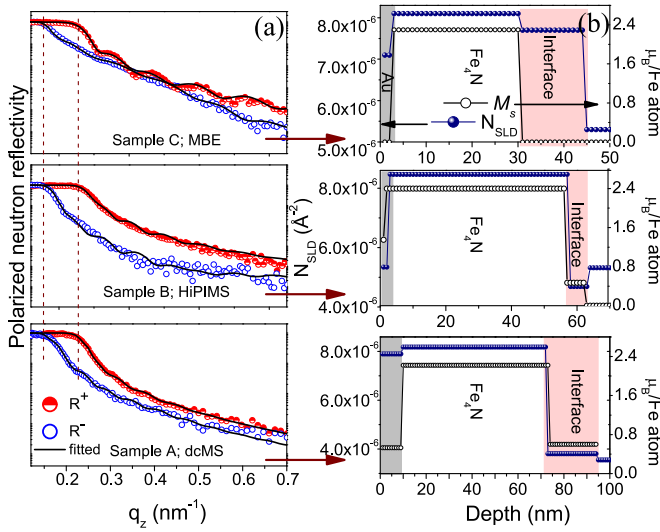
FIG. 6. Fitted PNR patterns (a) and corresponding N_{SLD} and magnetic depth profiles (b) of samples A, B, and C shown by an arrow.

roughness of the dcMS grown sample is much higher and in agreement with AFM results shown in the Supplemental Material [43].

The consequence of such a film-substrate interface is also expected to affect the magnetization behavior. Since the width of this interface was lowest in the HiPIMS grown sample, the value of magnetization was largest. However, from bulk magnetization measurements, contributions from the interface layer cannot be separated. Therefore, we did PNR measurements in samples A, B, and C. It is well known that the magnetic depth profile can be uniquely obtained from PNR measurements but it was surprising to note that they have not been performed in Fe$_4$N thin films before. Figure 6(a) shows the PNR patterns for sample A, B, and C and they were fitted using GenX software [52]. It is known that the splitting between spin-up (R$^+$) and -down (R$^-$) neutron reflectivities near the critical angle (q_c) is proportional to the magnetization of the sample, given by [53]:

$$q_c^{\pm} = \sqrt{(16\pi N(b_n \pm b_m)} \qquad (3)$$

where N is the number density, and b_n and b_m are the nuclear and magnetic scattering lengths for neutrons. We can see that at q_c the separation between R$^+$ and R$^-$ is somewhat larger in sample B, indicating higher M_s in this sample. Taking inputs from SIMS and XRR measurements, we again used a three-layer model described above and we can see that a film-substrate interface of similar thickness was present in all three samples. From the fitting of PNR data, we found that this interface layer is magnetically dead as shown in Fig. 6(b). The extent of this layer was about 20, 7, and 15 nm in dcMS, HiPIMS, and MBE grown samples, respectively. For the Fe$_4$N layer (excluding surface and interface), we obtained $M_s = 1.8, 2.4,$ and $2.1 (\pm 0.05) \mu_B$/Fe, respectively, for samples A, B, and C. This difference in values of M_s is in agreement with bulk magnetization results. This value of M_s matches well with the theoretical value in sample B (see Table I) but smaller values in samples A and C can be understood due to

the presence of the La impurity. Clearly, the microstructure and La diffusion affect M_s in Fe$_4$N thin films. As can be seen from SIMS depth profiles, La diffusion can prolong to a much larger length scale and thereby affects the M_s. Since in HiPIMS grown film the La diffusion could be suppressed due to a denser microstructure, the value of M_s reaches to the theoretically predicted value of $\approx 2.4\mu_B$/Fe [7]. Obtained results can be applied to understand very large differences in the magnetization of Fe$_4$N films studied in the literature as shown in Table I. It can be anticipated that interdiffusion can also take place from other substrates, e.g., Si, SrTiO$_3$, and MgO into Fe$_4$N (or any other film) and in this situation, the randomly generated interface may lead to the randomness in the values of M_s that can be seen in Fe$_4$N films grown in different works [14–19,28].

C. Elemental-specific magnetization

Theoretical calculations suggest a small but oppositely aligned moment at the N site in Fe$_4$N . The origin of such a magnetic moment was explained in terms of the extension of spin-down electron wave function near the interstitial region using spin-density plots located within the muffin-tin spheres [54–56].

However, to the best of our knowledge, experimentally the magnetic moment at the N site has only been studied by Ito *et al.* using XMCD measurements, but a large discrepancy between the theoretically simulated and experimentally observed N *K*-edge spectra can also be seen there [29]. In the present case, as we have shown that the Fe$_4$N sample grown using HiPIMS was superior and it will be interesting to inspect the electronic and magnetic behavior at Fe and N sites.

We performed XAS and XMCD measurements at Fe *L* edges at 300 K under UHV conditions by switching the applied external magnetic field ± 0.5 T (μ^+ and μ^-) along the direction of propagation of x-ray beam leaving the x-ray helicity unchanged. They are shown in Fig. 7(a), here edges appearing at photon energies of about 707 and 720 eV can be seen and assigned to Fe L_3 and L_2, respectively. A shoulder (marked by the ⋆) can also be seen about 3 eV above the L_3 edge and is more pronounced in sample B grown using HiPIMS. It may be noted here that such shoulder has been observed in some metallic ferromagnetic systems and has been explained in terms of the unoccupied single-particle density of states [29]. Here, this feature (⋆) can be attributed to the dipole transition from the Fe 2p core-level to the hybridized state σ^* between Fe (II) sites [43] and N 2p orbitals [19,21,29]. Since this feature (⋆) is noticeable only in sample B, it indicates that the HiPIMS grown sample has more localized states which could be due to better quality Fe$_4$N film. Distinct MCD spectra were observed at Fe *L* edges in all samples. Spin and orbital magnetic moments of samples A, B, and C were deduced by applying sum-rules analysis. The pre and post-edge background corrections were applied using Athena software [57]. Transitions to the continuum states were removed by subtracting the XAS average data using a two-step arctangent function.

It is known that, in sum-rules analysis, the magnetic moment is proportional to the number of holes (N_h) and in the present case, we used $N_h = 3.88$. This value was derived by
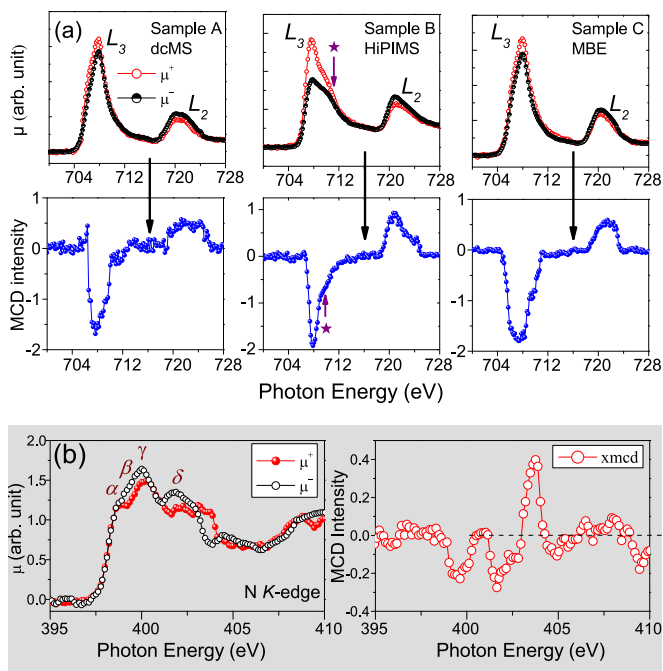
FIG. 7. XAS and XMCD spectra of samples A, B, and C observed at 300 K at (a) Fe L edge and (b) N K edge. The external magnetic field of ± 0.5 T was applied along the x-ray incidence direction to the sample surface.

Takagi *et al.* [21] for *in situ* grown Fe$_4$N thin films on a Cu substrate. Obtained values of spin (m$_S$), orbital (m$_L$), and total magnetic moment (m$_{tot}$) are shown in Table II along with the gyromagnetic ratio (m$_L$/m$_S$) for samples A, B, and C. Our values of m$_L$/m$_S$ matched well with the previously obtained values [19,21,29]. Here, the total magnetic moment including orbital and spin magnetic moments are the lowest obtained for sample A (dcMS), while the highest for sample B (HiPIMS), and are in agreement with bulk and PNR measurements.

We also did N K-edge XAS and XMCD measurements in sample B (HiPIMS) as shown in Fig. 7(b). Here, mainly four features can be seen and they are assigned as α, β, γ, and δ. The feature α is attributed to the dipole transition from the N 1s to π^* antibonding states and features β and γ are explained by σ^* antibonding states of N 2p and Fe 3d [19,29]. Moreover, distinct XMCD spectrum observed at N K edge confirms that N 2p orbital of Fe$_4$N is spin polarized. It is also interesting to note that the μ^+ and μ^- intensities get reversed compared to the Fe L_3-edge XMCD signal. This can be understood in

TABLE II. Results of the sum-rule analysis of Fe$_4$N films (sample A, B and C). Average spin (m$_S$), orbital (m$_L$), total (m$_{tot}$) magnetic moments, gyromagnetic ratio (m$_L$/m$_S$) of Fe are given.

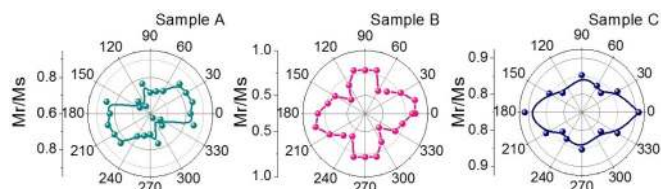| Sample	m$_S$ μ_B ± 0.1	m$_L$ μ_B ± 0.05	m$_{tot}$ μ_B/Fe	m$_L$/m$_S$
A	1.56	0.07	1.64	0.046
B	2.23	0.13	2.36	0.058
C	1.86	0.07	1.92	0.042

FIG. 8. Polar plot of squareness (M$_r$/Ms) with the applied field angle of samples A, B, and C.

terms of the oppositely aligned (negative) moment at the N site compared to the Fe, predicted theoretically [54–56]. Also, our N K-edge XMCD spectra are well consistent with the theoretically simulated spectra of Ito *et al.* [19].

D. Magnetic anisotropy

We did longitudinal MOKE measurements to study magnetic anisotropy (MA) and the polar plots of reduced remanence (M$_r$/M_s; here M$_r$ and M_s is the remanence and saturation magnetization) are shown in Fig. 8. As can be seen there, MA appears different in these three samples. Only sample B (HiPIMS) demonstrates a biaxial MA that is generally expected in cubic symmetry. Around the easy magnetization axes (100), the reduced remanence is highest close to 1(0.85) and around to the hard magnetization axes (110) it is close to cos 45° ≃ 0.52. Besides, a very weak biaxial MA can be seen for sample C. On the contrary, sample A exhibits a small uniaxial MA. Unusual behavior of MA found in sample A and C may be due to the significant diffusion of La from the substrate to the film or due to substrate-induced effect. Here also, a discrepancy in MA is evident, similar to the magnetization of samples A, B, and C. However, a detailed investigation is needed to further understand such behavior of MA.

As the biaxial MA can only be seen in sample B, the magnetization reversal by 90° domain is expected to appear in this sample. Therefore, Kerr images were captured between easy and hard axes for an applied field angle of 30° in the transverse direction. The MH hysteresis loops in longitudinal and transverse directions for applied field angle of 30° are shown in Fig. 9. Images were captured for the transversal M-H loop at points $a(=e)$, b, c, and d. The cusp at points b and d in both longitudinal and transversal directions reflects the 90° domain wall driven transition. 180° magnetization
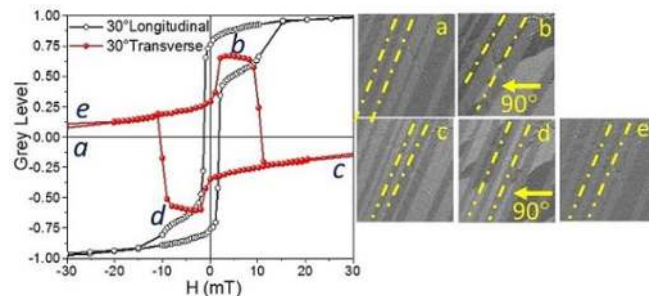

FIG. 9. Kerr domain images captured in between easy and hard axis of sample B at 30° in transversal and longitudinal directions.

reversal can be clearly seen from the image *a* to *e* followed by two consecutive $90°$ domain wall nucleation in image *b* and *d* (shown by arrow $90°$). However, stripe domains called a lamellar pattern can be seen in all images (shown by dashed lines in all images). Such lamellar pattern domains originate as ferroelectric domain arising due to the occurrence of twin structures in LAO [58].

IV. CONCLUSION

In conclusion, we made an attempt to resolve the anomaly about M_s values of Fe_4N thin films reported so far. In this view, we have grown epitaxial Fe_4N thin films on the LAO substrate by utilizing three different processes dcMS, MBE, and HiPIMS and investigated their structural and magnetic properties. M_s of these samples were measured using bulk magnetization, XMCD, and PNR measurements. Surprisingly, different M_s values were found for all samples. However, the highest value of M_s was achieved for the HiPIMS grown sample. Our SIMS results elucidate that the M_s in Fe_4N highly influenced by La diffusion through grain boundary. Detailed structural and magnetic depth profiling reveal that the denser microstructure may prohibit the La diffusion inside the film, resulting in a narrower film-substrate interface, found for HiPIMS grown sample. Similarly, the magnetic anisotropy behavior was also found to be different in all samples. Biaxial magnetic anisotropy expected for cubic symmetry was only observed for HiPIMS grown sample. However, the origin of different kinds of magnetic anisotropy requires a detailed investigation.

[1] S. Wolf, D. Awschalom, R. Buhrman, J. Daughton, S. Von Molnar, M. Roukes, A. Y. Chtchelkanova, and D. Treger, Science **294**, 1488 (2001).

[2] R. Wiesendanger, Nat. Rev. Mater. **1**, 16044 (2016).

[3] T. Jungwirth, X. Marti, P. Wadley, and J. Wunderlich, Nat. Nanotechnol. **11**, 231 (2016).

[4] R. Skomski, J. Phys.: Condens. Matter **15**, R841 (2003).

[5] C. Dennis, R. Borges, L. Buda, U. Ebels, J. Gregg, M. Hehn, E. Jouguelet, K. Ounadjela, I. Petej, I. Prejbeanu *et al.*, J. Phys.: Condens. Matter **14**, R1175 (2002).

[6] L. Falicov, D. T. Pierce, S. Bader, R. Gronsky, K. B. Hathaway, H. J. Hopster, D. N. Lambeth, S. Parkin, G. Prinz, M. Salamon *et al.*, J. Mater. Res. **5**, 1299 (1990).

[7] E. L. P. y. Blancá, J. Desimoni, N. E. Christensen, H. Emmerich, and S. Cottenier, Phys. Status Solidi (B) **246**, 909 (2009).

[8] M. Meinert, J. Phys.: Condens. Matter **28**, 056006 (2016).

[9] S. Kokado, N. Fujima, K. Harigaya, H. Shimizu, and A. Sakuma, Phys. Rev. B **73**, 172410 (2006).

[10] B. Yang, L. Tao, L. Jiang, W. Chen, P. Tang, Y. Yan, and X. Han, Phys. Rev. Appl. **9**, 054019 (2018).

[11] L. Yin, W. Mi, and X. Wang, Phys. Rev. Appl. **6**, 064022 (2016).

[12] L. Yin, X. Wang, and W. Mi, ACS Appl. Mater. Interfaces **9**, 15887 (2017).

[13] H. Li, G. Wang, D. Li, P. Hu, W. Zhou, S. Dang, X. Ma, T. Dai, S. Kang, F. Yu *et al.*, ACS Appl. Mater. Interfaces **11**, 16965 (2019).

[14] S. Atiq, H.-S. Ko, S. A. Siddiqi, and S.-C. Shin, Appl. Phys. Lett. **92**, 222507 (2008).

[15] J. Feng-Xian, Z. Ye, Z. Guo-Wei, Z. Jun, F. Jiu-Ping, and X. Xiao-Hong, Chin. Phys. Lett. **32**, 087501 (2015).

[16] I. Dirba, M. B. Yazdi, A. Radetinac, P. Komissinskiy, S. Flege, O. Gutfleisch, and L. Alff, J. Magn. Magn. Mater. **379**, 151 (2015).

[17] R. Loloee, K. Nikolaev, and W. Pratt, Jr., Appl. Phys. Lett. **82**, 3281 (2003).

[18] Y. Na, C. Wang, J. Xiang, N. Ji, and J. ping Wang, J. Cryst. Growth **426**, 117 (2015).

[19] K. Ito, G. H. Lee, K. Harada, M. Suzuno, T. Suemasu, Y. Takeda, Y. Saitoh, M. Ye, A. Kimura, and H. Akinaga, Appl. Phys. Lett. **98**, 102507 (2011).

[20] K. Nikolaev, I. Krivorotov, E. Dahlberg, V. Vas' ko, S. Urazhdin, R. Loloee, and W. Pratt, Jr., Appl. Phys. Lett. **82**, 4534 (2003).

[21] Y. Takagi, K. Isami, I. Yamamoto, T. Nakagawa, and T. Yokoyama, Phys. Rev. B **81**, 035422 (2010).

[22] D. Gölden, E. Hildebrandt, and L. Alff, J. Magn. Magn. Mater. **422**, 407 (2017).

[23] H. Li, X. Li, D. Kim, G. Zhao, D. Zhang, Z. Diao, T. Chen, and J.-P. Wang, Appl. Phys. Lett. **112**, 162407 (2018).

[24] W. Mi, Z. Guo, X. Feng, and H. Bai, Acta Mater. **61**, 6387 (2013).

[25] W. Mi, X. Feng, X. Duan, H. Yang, Y. Li, and H. Bai, Thin Solid Films **520**, 7035 (2012).

[26] Y. Imai, Y. Takahashi, and T. Kumagai, J. Magn. Magn. Mater. **322**, 2665 (2010).

[27] V. Adhikari, Z. Liu, N. Szymanski, I. Khatri, D. Gall, P. Sarin, and S. Khare, J. Phys. Chem. Solids **120**, 197 (2018).

[28] J. L. Costa-Krämer, D. M. Borsa, J. M. García-Martín, M. S. Martín-González, D. O. Boerma, and F. Briones, Phys. Rev. B **69**, 144402 (2004).

[29] K. Ito, K. Toko, Y. Takeda, Y. Saitoh, T. Oguchi, T. Suemasu, and A. Kimura, J. Appl. Phys. **117**, 193906 (2015).

[30] A. Narahara, K. Ito, T. Suemasu, Y. Takahashi, A. Ranajikanth, and K. Hono, Appl. Phys. Lett. **94**, 202502 (2009).

[31] Y. Komasaki, M. Tsunoda, S. Isogami, and M. Takahashi, J. Appl. Phys. **105**, 07C928 (2009).

[32] A. Anders, J. Appl. Phys. **121**, 171101 (2017).

[33] J. Gudmundsson, N. Brenning, D. Lundin, and U. Helmersson, J. Vac. Sci. Technol., A **30**, 030801 (2012).

[34] K. Strijckmans, F. Moens, and D. Depla, J. Appl. Phys. **121**, 080901 (2017).

[35] J. Stahn and A. Glavic, Nucl. Instrum. Methods Phys. Res., Sect. A **821**, 44 (2016).

[36] J. Stahn and A. Glavic, J. Phys.: Conf. Ser. **862**, 012007 (2017).

[37] S. Mattauch, A. Koutsioubas, U. Rücker, D. Korolkov, V. Fracassi, J. Daemen, R. Schmitz, K. Bussmann, F. Suxdorf, M. Wagener *et al.*, J. Appl. Crystallogr. **51**, 646 (2018).

[38] D. M. Phase, M. Gupta, S. Potdar, L. Behera, R. Sah, and A. Gupta, in *Proceedings of the 58th DAE Solid State Physics Symposium 2013*, edited by C. Murli, D. Bhattacharyya, and S. C. Gadkari, AIP Conf. Proc. No. 1591 (AIP, New York, 2014), p. 685.

[39] Z. Wang and A. Shapiro, Surf. Sci. **328**, 141 (1995).

[40] M. Norton and J. Bentley, J. Mater. Sci. Lett. **15**, 1851 (1996).

[41] R. Ciancio, A. Vittadini, A. Selloni, R. Arpaia, C. Aruta, F. M. Granozio, U. S. Di Uccio, G. Rossi, and E. Carlino, J. Nanopart. Res. **15**, 1735 (2013).

[42] M. Lagally, D. Savage, and M. Tringides, *Diffraction from disordered surfaces: An overview, in Reflection High Energy Electron Diffraction and Reflection Electron Imaging of Surfaces*, edited by P. K. Larsen and P. J. Dobson (Springer US, Boston, MA, 1988), pp. 139–174.

[43] See Supplemental Material at http://link.aps.org/supplemental/10.1103/PhysRevMaterials.3.114414 for describing the morphology, microstrcutre, and growth mode Fe_4N thin films.

[44] A. Tayal, M. Gupta, A. Gupta, P. Rajput, and J. Stahn, Phys. Rev. B **92**, 054109 (2015).

[45] P. Fielitz, G. Borchardt, M. Schmücker, and H. Schneider, Solid State Ionics **160**, 75 (2003).

[46] I. Kaur, W. Gust, and Y. Mishin, *Fundamentals of Grain and Interphase Boundary Diffusion* (Wiley, New York, 1995).

[47] S. Harton, F. Stevie, and H. Ade, Macromolecules **38**, 3543 (2005).

[48] S. Harton, F. Stevie, and H. Ade, J. Vac. Sci. Technol., A **24**, 362 (2006).

[49] S. A. Chambers, Surf. Sci. **605**, 1133 (2011).

[50] H. Kawanowa, H. Ozawa, M. Ohtsuki, Y. Gotoh, and R. Souda, Surf. Sci. **506**, 87 (2002).

[51] C. Braun, *Parratt32- The Reflectivity Tool* (v 1.6) (HMI Berlin, Berlin, 1997).

[52] M. Björck and G. Andersson, J. Appl. Crystallogr. **40**, 1174 (2007).

[53] S. J. Blundell and J. A. C. Bland, Phys. Rev. B **46**, 3391 (1992).

[54] M. Sifkovits, H. Smolinski, S. Hellwig, and W. Weber, J. Magn. Magn. Mater. **204**, 191 (1999).

[55] J. M. Coey, *Magnetism and Magnetic Materials* (Cambridge University Press, Cambridge, 2009).

[56] G. Scheunert, O. Heinonen, R. Hardeman, A. Lapicki, M. Gubbins, and R. Bowman, Appl. Phys. Rev. **3**, 011301 (2016).

[57] B. Ravel and M. Newville, J. Synchrotron Radiat. **12**, 537 (2005).

[58] Z. Hussain, D. Kumar, and V. R. Reddy, J. Magn. Magn. Mater. **151**, 61 (2019).